Polymer Testing 152 (2025) 108987

Contents lists available at ScienceDirect

Polymer Testing

journal homepage: www.elsevier.com/locate/polytest

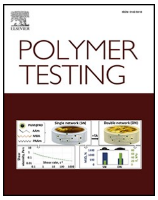

Optimizing *p*-aramid copolymer superfibers: The synergistic effect of solution rheology and fiber structure

Jaegeun Lyu[a,1], Hyeonjeong Kim[b,1], Min Woo Kim[a], Juyoung Kim[a], Howon Choi[c], Donghoon Lee[a], Daeyoung Lim[d], Ji Ho Youk[c,*], Youngho Eom[b,**], Han Gi Chae[a,***]

[a] *Department of Materials Science and Engineering, Ulsan National Institute of Science and Technology (UNIST), Ulsan, 44919, South Korea*
[b] *Department of Organic and Nano Engineering, Human-Tech Convergence Program, Hanyang University, Seoul, 04763, South Korea*
[c] *Department of Chemistry and Chemical Engineering, Education and Research Center for Smart Energy and Materials, Inha University, Incheon, 22212, South Korea*
[d] *Material and Component Convergence R&D Department, Korea Institute of Industrial Technology (KITECH), Ansan, 15588, South Korea*

ARTICLE INFO

Keywords:
p-aramid copolymer
3,4′-oxydianiline
Superfibers
Rheology

ABSTRACT

Para-aramid (*p*-aramid) fibers have gained significant attention in lightweight vehicle and optical cable industries. However, the use of harsh sulfuric acid-based processing limits their widespread adoption. As a promising alternative, p-aramid copolymer (*p*-AC) offers improved processability while maintaining comparable properties. In this study, *p*-AC superfibers incorporating 3,4′-oxydianiline (3,4′-ODA) monomers were successfully fabricated through optimized manufacturing processes spanning from solution preparation to fiber property enhancement. The homogeneity of spinning solutions, determined by polymerization conditions, serves as a key factor governing fiber structure and properties. Three *p*-AC solutions with varying rheological homogeneities, classified as low (L), moderate (M), and high (H), exhibited Cole-Cole plot slopes of 1.12, 1.34, and 1.65, respectively. A higher solution homogeneity enabled greater draw ratios, leading to more compact and well-aligned fiber microstructures. Consequently, as the homogeneity increased, the fiber crystallinity and orientation factor increased from 56.1 % and 0.923 to 62.2 % and 0.968, respectively. Notably, the *p*-AC-H fibers exhibited tensile modulus and strength of 82.4 and 3.1 GPa, respectively, representing 11.2 % and 41.0 % increases compared to those of *p*-AC-L fibers (74.1 and 2.2 GPa, respectively). These findings establish a direct correlation between solution homogeneity and fiber performance, providing a theoretical background for the precise design of high-performance superfibers.

1. Introduction

The surging demand for high-performance fibers in advanced industries, such as aerospace, automotive, and defense, has drawn significant attention to superfibers, including para-aramid (*p*-aramid) and carbon fibers [1–3]. These fibers are favored not only for their exceptional mechanical strength, thermal resistance, and chemical stability but also for their lightweight nature, which is critical for performance-driven applications [4–6]. The superior physical properties of these fibers originate from their strong intermolecular interactions (such as hydrogen bonding, dipole–dipole bonding, and π–π stacking), extremely high molecular weight, and/or from the rigidity of their molecular backbones [1–6]. While these structural characteristics confer excellent high mechanical properties, they also render polymers thermally infusible, making conventional melt processing nearly impossible. Accordingly, most of these superfibers or their precursors must be processed via wet spinning.

High-performance polymers, including *p*-aramid and polyacrylonitrile (a precursor to carbon fibers), require dissolution in strong acids or highly polar organic solvents [7,8]. However, owing to the persistence of strong intermolecular interactions in solutions, controlling the solution properties is extremely challenging. This complexity highlights the crucial need to understand and precisely control the polymer–solvent interactions in the wet spinning process of

---

[*] Corresponding author.
[**] Corresponding author.
[***] Corresponding author.
E-mail addresses: youk@inha.ac.kr (J.H. Youk), eomyh@hanyang.ac.kr (Y. Eom), hgchae@unist.ac.kr (H.G. Chae).
[1] These authors have contributed equally to the work.

https://doi.org/10.1016/j.polymertesting.2025.108987
Received 30 June 2025; Received in revised form 1 September 2025; Accepted 16 September 2025

high-performance fibers. In particular, *p*-aramid exhibits liquid crystalline behavior owing to its rigid chain backbone and strong intermolecular interactions, which further complicates the control of solution spinnability during the wet spinning process [9,10]. The lyotropic liquid crystalline polymer undergoes a series of phase transitions with increasing concentration, typically progressing from isotropic to biphasic, to anisotropic sol, and finally to anisotropic gel [11]. Among these phases, the liquid crystalline fiber spinning is recommended only for the anisotropic sol phase [12]. However, this phase exists within a narrow concentration window, making it difficult to determine the optimal spinning concentration [12].

Significant efforts have been devoted to converting the liquid crystalline phases of *p*-aramid solutions into isotropic phases without substantially compromising the superior performance of the resulting fibers. This has been accomplished through molecular tuning strategies such as reducing chain regularity (e.g., para to meta substitution) [13], introducing side group substitution [14,15], and employing copolymerization approaches [16]. Among these, *p*-aramid copolymer (*p*-AC), synthesized using 3,4′-oxydianiline (3,4′-ODA) as a third co-monomer, has emerged as one of the most promising alternatives to conventional *p*-aramid. This offers significantly improved processability while maintaining comparable fiber properties [17]. The introduction of a kink moiety on the backbone disrupts the chain regularity, enabling *p*-AC to dissolve in an organic solvent such as N-methyl-2-pyrrolidone (NMP), resulting in isotropic solutions. The spinnability of these isotropic solutions is primarily affected by their viscoelasticity and homogeneity [18,19]. Despite the absence of liquid crystalline domains, attention must still be paid to controlling the solution properties of *p*-AC, as the polymer forms strong intermolecular hydrogen bonds that can lead to heterogeneous deterioration of the isotropic solution.

In this study, we highlight the critical relationship between the rheological properties of the solution, the resulting fiber structure, and the tensile properties of *p*-AC fibers. The fiber fabrication process involves spinning dope preparation via polymerization, neutralization, dry-jet wet spinning, and post-heat drawing. *p*-AC spinning dopes with varying degrees of homogeneity were prepared by modifying the neutralization conditions. As the extent of neutralization increases, the solution transitions from opaque to transparent, indicating improved homogeneity. Consequently, the solution homogeneity significantly influenced the processability of the fibers, including their spinnability and drawability. Establishing a clear correlation between the solution properties and fiber performance provides a theoretical foundation for producing high-performance fibers that meet the growing demands of advanced industries.

2. Experiment

2.1. Materials

p-Phenylenediamine (PPD, Amino-Chem), 3,4′-ODA (Wakayama Seika Kogyo), terephthaloyl chloride (TPC, >99 %, Sigma-Aldrich), anhydrous NMP (>99.5 %, Sigma-Aldrich), and calcium hydroxide ($Ca(OH)_2$, >95 %, Sigma-Aldrich) were used as received.

2.2. Synthesis of p-AC

A series of *p*-AC were synthesized through a direct polycondensation reaction using a mixture of PPD and 3,4′-ODA as diamines and TPC as a diacid. For the synthesis of the three types of *p*-AC solutions, a 2 L, dual-jacketed, four-neck flask reactor was utilized within a nitrogen-filled glove box. The reactor was charged with 10.1 g of PPD (93.44 mmol), 18.71 g of 3,4′-ODA (93.44 mmol), and 450 mL of NMP. The mixture was then stirred at 25 °C under a continuous flow of dry nitrogen to ensure complete dissolution of all reactants. Subsequently, 37.94 g of powdered TPC (186.88 mmol) was rapidly added to the reactor. For the neutralization process, the temperature of the polymer solution was raised to 80 °C and a dispersion of 13.85 g of $Ca(OH)_2$ (186.88 mmol) in 45 mL of NMP was quickly added to the *p*-AC solutions. Fig. 1(a) illustrates a detailed profile of the reaction temperature and timing of neutralization using $Ca(OH)_2$. This process ultimately resulted in polymer solutions with a concentration of 9.0 wt%, which exhibited different transparencies depending on the neutralization time (Fig. 1(b)). The solution grade was divided into low (L), moderate (M), and high (H) grades based on the transmittance intensity, which affected the rheological properties of the solution and fiber properties in an identical trend. The solutions were named by *p*-AC-X (X = solution grade).

2.3. Fiber spinning

The entire fabrication process was based on the *p*-AC spinning process [20,21], which is a dry-jet wet spinning process that involves two steps (Fig. 1(c)); spinning the *p*-AC solutions into a coagulation bath and heat drawing the as-spun fibers (Fig. 1(d)). The composition of the coagulation bath and washing bath was 100 % deionized water, and a three-layered bath was used to remove residual solvent from the coagulated fibers through a thorough washing process. The ratio between the solution extrusion speed and the take-up speed generally determines the draw ratio. The as-spun draw ratio (SDR) was set to take up the fibers in a stable state. The optimized SDR was 2.0 for all solutions. Suitable spinning temperatures for the solutions were estimated from the rheological data. Based on these data, the dope tank was packed with a heating jacket at the optimized temperature. The heat drawing process involved passing as-spun fibers through a heating furnace at 460 °C, and the post-drawing process was carried out with a maximum draw ratio to ensure stable drawing (Table S1). The TDR was determined using SDR and post-draw ratio (PDR) (TDR = SDR × PDR).

2.4. Characterization

The molecular characterization of the synthesized *p*-AC was conducted using gel permeation chromatography (GPC, Young Lin Chrozen HPLC system). This analysis determined the number-average molecular weight (M_n) and polydispersity index (PDI) of the *p*-AC. A 0.01 M LiBr/NMP solution was used as the mobile phase, maintained at 80 °C with a flow rate of 1.0 mL/min. Poly(methyl methacrylate) standards were used for column calibration. The hydrodynamic diameter of 0.1 mg mL^{-1} *p*-AC solutions was measured by dynamic light scattering (DLS, Zetasizer Nano ZS, Malvern, UK) at 25 °C. UV–vis transmittance spectra were measured for *p*-AC solutions diluted to 0.1 wt% in additional NMP using a Cary 5000 (Agilent) at 25 °C. The rheological properties of *p*-AC solutions were characterized using a stress-controlled rotational rheometer (MCR 302e, Anton Paar, Austria) with a concentric cylinder geometry. For a precise measurement, 4.0 mL of the solution was poured into the cylinder, which could fill the entire cup when the rotor was dipped into the cup. Dynamic frequency sweeps were conducted in an angular frequency range of 0.05–500 $rad\bullet s^{-1}$ at 20–80 °C in 10 °C intervals and a strain level of 5 %. The surface and cross-section morphology of the *p*-AC fibers were examined using field-emission scanning electron microscopy (FE-SEM, SU-8220, Hitachi) at an accelerating voltage of 10 kV. The samples were prepared using an ion sputter (E−1045, Hitachi) with a platinum coating. The cross-sections of the fibers were prepared after tensile testing. To calculate the diameter and circularity of the fibers, cross-section images of the fibers were captured using an optical microscope (DM2500 M, Leica). The ImageJ software program was used to analyze the circularity and diameter. The tensile properties of *p*-AC fibers were evaluated using a single filament tensile tester (FAVIMAT+, Textechno) at a gauge length of 25.4 mm and a strain rate of 1 %/s with a pretension of 0.5 cN/tex. The linear density was measured using a vibroscope before tensile testing, in accordance with ASTM D 1577. The resonance frequency of the sample was measured at a constant gauge length with a known pre-tension. The obtained data were used to calculate the linear density using formula T

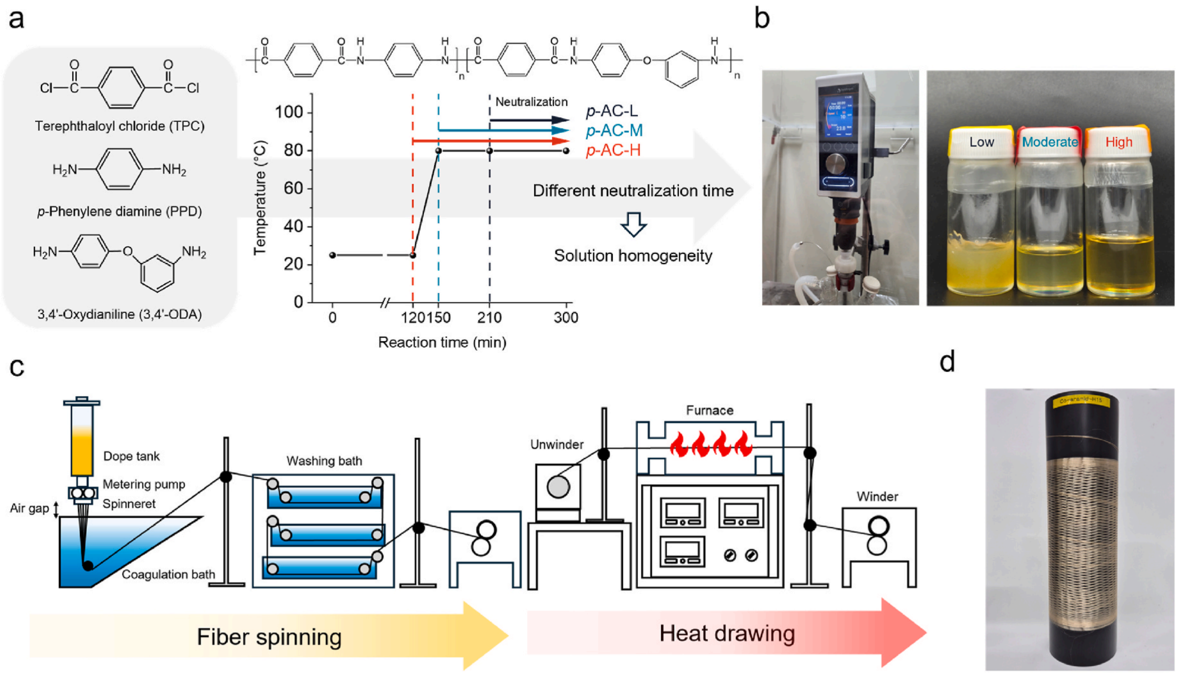

Fig. 1. Schematic representation of *p*-AC fiber production process. (a) Synthesis of *p*-AC solution with different neutralization times, (b) photograph of overhead stirrer and *p*-AC solutions (left: low, center: moderate, and right: high grade), (c) whole process of *p*-AC fiber from spinning to heat drawing and (d) photograph of *p*-AC fiber.

$= F/(4 \cdot f^2 \cdot L^2)$, where T = linear density, F = pretension force, f = resonance frequency, and L = test section length. Tensile testing was conducted using at least 10 filaments for each specimen.

Wide angle X-ray diffraction (WAXD) and Small angle X-ray scattering (SAXS) were performed at the PLS-II 6D UNIST-PAL beamline of the Pohang Accelerator Laboratory in Pohang, Republic of Korea. The energy of the X-rays was 18.986 and 11.564 keV for WAXD and SAXS measurements, respectively. The distances between the detector and the sample were 240 mm and 3074 mm for WAXD and SAXS, respectively. Data were analyzed using the Peakfit software program. From the WAXD analysis, the crystallinity and Herman's orientation factor were measured [22–24]. By deconvoluting crystalline and amorphous peaks in 1D WAXD profiles, the crystallinity of the *p*-AC fibers was obtained, and the orientation factor (f) was calculated using azimuthal scan at 2θ ~ 42.5° (006) plane peak by Wilchinsky equation,

$$f = \frac{3 < cos^2 \phi > -1}{2} \tag{1}$$

$$< cos^2 \phi > = \frac{\int_0^{\frac{\pi}{2}} I(\phi) \, cos^2 \phi \, sin \, \phi \, d\phi}{\int_0^{\frac{\pi}{2}} I(\phi) \, sin \, \phi \, d\phi} \tag{2}$$

where ϕ is the azimuthal angle, and I is the intensity. In addition, the misorientation angle between the crystalline fibril and the fiber axis direction was defined by SAXS analysis using the Ruland streak method [25]. The azimuthal scan was represented as a function of s in reciprocal space and characterized based on the observed integral breadth (B_{obs}).

$$B_{obs} = \frac{\int_{\varphi_{max}-\frac{\pi}{2}}^{\varphi_{max}+\frac{\pi}{2}} I(s,\varphi) d\varphi}{I(s,\varphi_{max})} \tag{3}$$

$$s^2 B_{obs}^2 = \frac{1}{l_f^2} + s^2 B_g^2 \tag{4}$$

$I(s,\varphi)$ in azimuthal scan is obtained at scattering vector, where s is the scattering vector defined as $s = 2 \sin \theta / \lambda$, with $2\ \theta$ representing the scattering angle and λ denoting the wavelength. φ_{max} refers to the angle at which the maximum peak of the azimuthal scan is indicated. B_g represents the actual width of the orientation distribution, which is a measure of the preferred alignment of the microfibrils with respect to the fiber axis.

The dimensional stability of *p*-AC fibers was measured by dynamic mechanical analysis (DMA) with Q800 (TA Instruments) at 25 °C. A creep test under constant stress was performed at 40 % tensile strength, maintaining the stress for 100 min. A cyclic test was conducted at 50 % tensile strength with a 20 %/min ramp stress. Each cycle lasted approximately 150 s. Both tests were conducted at 25 °C and with a pre-tension of 2 % tensile strength to prevent the over-release of the fibers.

The thermal stability was measured using thermogravimetric analysis (TGA) from 25 °C to 800 °C with a ramp rate of 5 °C/min in air on a Q500 (TA Instruments).

3. Results and discussion

3.1. Effect of neutralization time on p-AC solution properties and fiber fabrication

In contrast to *p*-aramid homopolymers, which exhibit liquid crystalline behavior, organo-soluble *p*-AC forms isotropic solutions [26]. Despite their isotropic nature, their solution properties and homogeneity are highly dependent on the polymerization conditions (Fig. 1(a) and (b)). When TPC is added to a solution of PPD and 3,4′-ODA in NMP, polymerization proceeds rapidly, causing a sharp increase in the viscosity of the reactant. During this process, amide bonds form through the reaction of the acyl chloride group in TPC with the amino group in PPD or 3,4′-ODA, producing hydrogen chloride (HCl) as a byproduct [27,28]. Because the byproduct can reduce the molecular weight of *p*-AC, it should be neutralized using $Ca(OH)_2$. This neutralization prevents acid-induced degradation of the aramid chains, maintains solution clarity by minimizing ionic aggregation, ensures rheological stability for fiber spinning, protects processing equipment from corrosion, and mitigates environmental and safety concerns associated with residual acid. Ca^{2+} and Cl^- ions play complementary roles in this process: Ca^{2+} ions interact favorably with NMP, likely enhancing its solvating power, while Cl^- ions act as strong hydrogen bond acceptors that disrupt the intermolecular hydrogen bonding between *p*-AC chains [29]. Similarly, the neutralization time had a significant impact on the molecular parameters and solution properties (Table S2). The *p*-AC-L solution with a neutralization time of 90 min exhibited a relatively low M_n of 133,700 g mol^{-1}. By contrast, the longer neutralization times of 150 and 180 min yielded higher M_ns of 208,100 and 195,800 g mol^{-1} for the *p*-AC-M and *p*-AC-H solutions, respectively. In addition, increasing the neutralization time reduced the PDI from 2.38 to 2.00. The comparable M_n and PDI values of *p*-AC-M and *p*-AC-H solutions indicate that the neutralization beyond 150 min was sufficient to suppress the acid-induced chain degradation. Conversely, insufficient neutralization rendered the *p*-AC-L solution opaque, as evidenced by its significantly lower transmittance compared with the other solutions (Fig. S1). To further clarify the relationship between solution properties and fiber performance, three *p*-AC fibers were fabricated via dry-jet wet spinning, followed by post-heat drawing at 460 °C.

3.2. Viscoelasticity and solution homogeneity of p-AC solutions

Beyond molecular parameters such as molecular weight and distribution, solution homogeneity is a critical factor governing both processability and resulting fiber properties. The presence of aggregates not only destabilizes the discharge behavior of the spinning solutions but also remains as structural defects in fibers [19]. The solution properties of *p*-AC were evaluated via rheological characterization (Fig. 2). In the dynamic viscosity (η') curves, *p*-AC solutions exhibited a lower Newtonian flow region, followed by shear thinning at high frequencies, a characteristic behavior of homogeneous polymer solutions (Fig. 2(a)) [15,30,31]. The extent of viscoelasticity (η' and storage modulus (G')) was closely related to M_n (Table S2). At 1.08 rad s^{-1}, the η' values for *p*-AC-L, *p*-AC-M, and *p*-AC-H were 110.0, 287.5, and 246.2 Pa s, respectively, while the corresponding G' values of 11.8, 54.7, and 31.7 Pa (Fig. 2(b) and (c)). Solution homogeneity can be quantified using Cole–Cole plot slope, which represents the logarithmic plot of G' versus the loss modulus (G'') [15,30,31]. In general, a slope close to 2.00 indicates greater homogeneity. The slopes for *p*-AC-L, *p*-AC-M, and *p*-AC-H were 1.12, 1.34, and 1.65, respectively (Fig. 2(d) and (e)), reflecting the effect of extended neutralization during polymerization. While the viscosity and storage modulus are correlated with M_n, the Cole–Cole slope reflects the trend of the neutralization time during polymerization. Notably, *p*-AC-H solutions exhibited significantly higher homogeneity compared to *p*-AC-M solutions, despite having similar M_n and rheological properties.

DLS analysis provides direct evidence for assessing the solution homogeneity by measuring the hydrodynamic diameter of polymer coils. The observed hydrodynamic diameters were 51.8, 37.1, and 33.0 nm for *p*-AC-L, -M, and -H, respectively (Fig. S2). The larger hydrodynamic diameter can be attributed to the presence of aggregates in solution [32,33]. In other words, the reduced diameter indicates improved solution homogeneity, which quantitatively supports the rheological analysis based on the Cole-Cole slope. A similar trend was observed in the flow relaxation time (τ_f), calculated as the reciprocal of the crossover frequency between G' and G'' [31,34] (Fig. 2(f)). The τ_f of *p*-AC-L was 0.027, indicating rapid recovery to equilibrium and polymer chain dynamics unfavorable for uniaxial stretching [35]. Therefore, *p*-AC-H solutions exhibit excellent spinnability, whereas *p*-AC-L solutions are less suitable for fiber spinning.

3.3. Morphology and uniformity of p-AC fibers

The structural uniformity of the *p*-AC fibers was evaluated by observing their cross-sectional and surface morphologies (Fig. 3). The draw ratio of each fiber sample is denoted by an "*x*" appended to the sample code, such as in *p*-AC-L*x*. *p*-AC-L2 exhibited a kidney-shaped cross-section, *p*-AC-H2 showed an elliptical shape, and *p*-AC-M2 displayed an intermediate morphology between the two (Fig. 3(a) and S3). Regarding the surface morphology, *p*-AC-L6 fibers exhibited considerable diameter variation, in contrast to the uniform diameters observed in

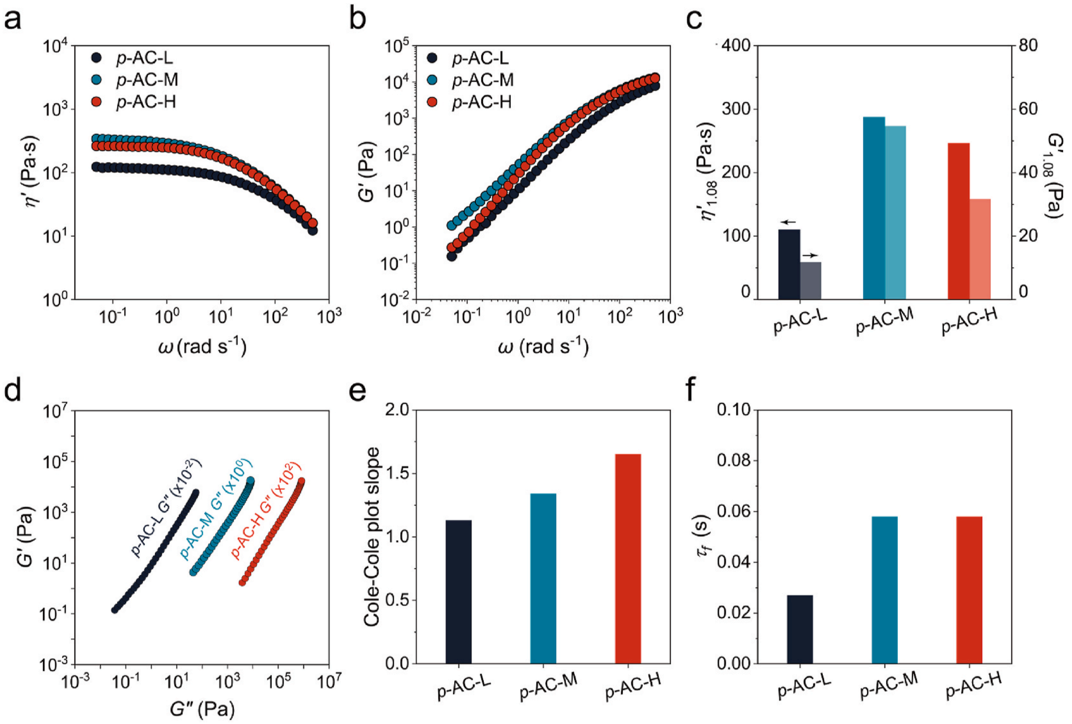

Fig. 2. Rheological properties of *p*-AC solutions at the spinning temperature. (a) Dynamic viscosity (η') and (b) storage modulus (G') depending on frequency sweep. (c) Quantitative values of η' and G' at 1.08 rad s^{-1}. (d) G' and loss modulus (G'') curves of the solutions shifted horizontally by multiplying arbitrary shift factors for more precise comparison, and (e) Cole–Cole plot slope of the *p*-AC solutions. (f) Relaxation time (τ_f) of the solutions.

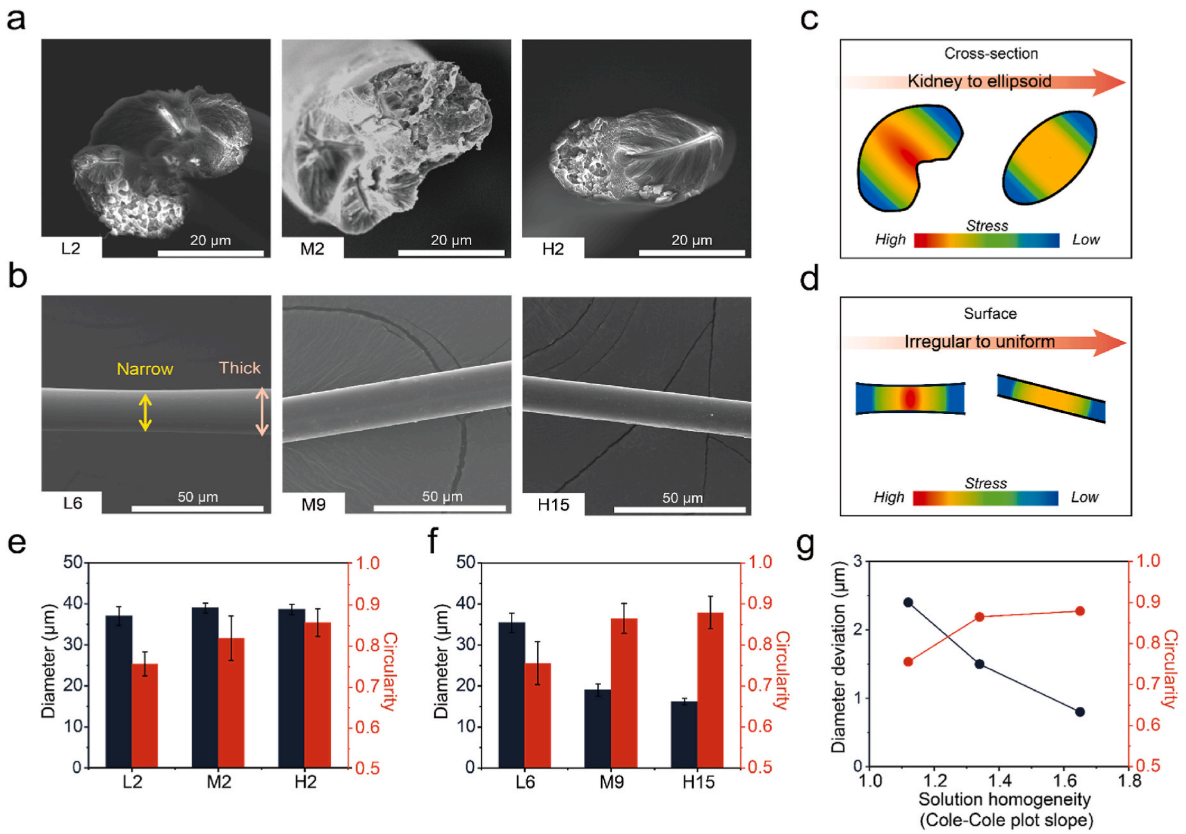

Fig. 3. Morphology analysis of *p*-AC fibers. (a) SEM cross-section images of as-spun fibers after tensile test and (b) surface images of post-drawn fiber. The degree of stress concentration when tensile force was activated, depending on the cross-section (c) and surface morphology (d). Quantitative value of diameter and circularity of (e) as-spun fiber and (f) post-drawn fiber. (g) Correlation of fiber morphology and solution homogeneity.

p-AC-M9 and *p*-AC-H15 fibers (Fig. 3(b)). In general, when fibers are subjected to strain, their stress dissipation behavior along the fiber axis is primarily governed by their structural uniformity. Fibers with lower structural uniformity, characterized by a kidney-shaped cross-section and/or significant diameter deviations (as observed in *p*-AC-L fibers), experienced localized stress concentrations at the edges of the kidney shape (in cross-sectional terms) or thinner regions along the fiber axis, thereby accelerating fracture initiation and propagation (Fig. 3(c) and (d)). As a result, the relatively non-uniform *p*-AC-L fibers exhibited limited stretchability, restricting their total draw ratio (TDR) to 6. Conversely, the superior structural uniformity of the *p*-AC-H fibers facilitated a higher degree of post-drawing owing to the evenly distributed stress, which resulted in a TDR of 15. The poor processability of *p*-AC-L fibers can be attributed mainly to their relatively low M_n compared to the other fibers.

Beyond the molecular weight influence, two quantitative parameters representing the structural uniformity such as diameter variation, and circularity of the fibers were calculated to draw a correlation with the Cole–Cole plot slopes (rheological parameter for solution homogeneity). The diameters and circularities of the *p*-AC fibers are shown in Fig. 3(e) and (f), and the correlations between the structural parameters of the post-drawn fibers and their solution homogeneity are displayed in Fig. 3 (g). It should be noted that the structural uniformities are enhanced (i.e., circularity increases and diameter deviation decreases) as the Cole–Cole slope increases. Based on these correlations, it can be concluded that solution heterogeneity leads to structural defects in the as-spun fibers, thereby dictating the TDR (i.e., stretchability).

3.4. *Microstructural analysis of p-AC fibers*

Along with the morphological aspects of the fibers, the effects of solution homogeneity on the microstructures were investigated using X-ray analyses. Fig. 4(a) illustrates the microfibril structures of the *p*-AC fibers at different zoomed-in scales. Highly oriented crystalline structures must be obtained through the heat-drawing process near the degradation temperature of *p*-AC fibers. Therefore, the as-spun fibers consist of incomplete internal structures, lower orientation factor, and lower crystallinity. While the heat-drawing process enhances the structural properties of the fibers, the optimal draw ratio depends on the morphology of the as-spun fibers. In general, the orientation factor and crystallinity, key indicators of structural quality, tend to increase with higher draw ratio [36].

A representative 2D WAXD pattern for *p*-AC-L6 is shown in Fig. 4(b), and the patterns of the other fibers are presented in Fig. S4**.** The corresponding 1D WAXD profiles of *p*-AC-L, *p*-AC-M, and *p*-AC-H fibers are shown in Fig. 4(c). In the 1D and 2D WAXD results, strong diffraction peaks appeared at 20.3° and 42.5°, corresponding to the (110) and (006) planes in the equatorial and meridional scans, respectively [37,38]. Although the overall pattern shapes were similar, the intensity and sharpness of the peaks varied with draw ratio. In the *p*-AC-L6 fibers, the characteristic peak corresponding to the (200) plane observed in *p*-aramid fibers produced by low draw ratios disappeared above a draw ratio of 9, indicating that the highly aligned molecular chains caused a structural transition from the (200) plane to the (110) plane. Based on the WAXD results (Fig. 4(d)), the calculated crystallinity and orientation factor of *p*-AC fibers indicate that they intrinsically exhibited high crystallinity (>56.1 %) and orientation factor (>0.923), attributed to their rigid chain molecules. Among them, the *p*-AC-H12 and *p*-AC-H15 fibers exhibited outstanding crystallinity (62.0 % and 62.2 %) and orientation factor (0.965 and 0.968). Specifically, the orientation factor is pretty close to unity, indicating a near-perfect orientation of the polymeric chains along the fiber axis. In contrast, the lowest

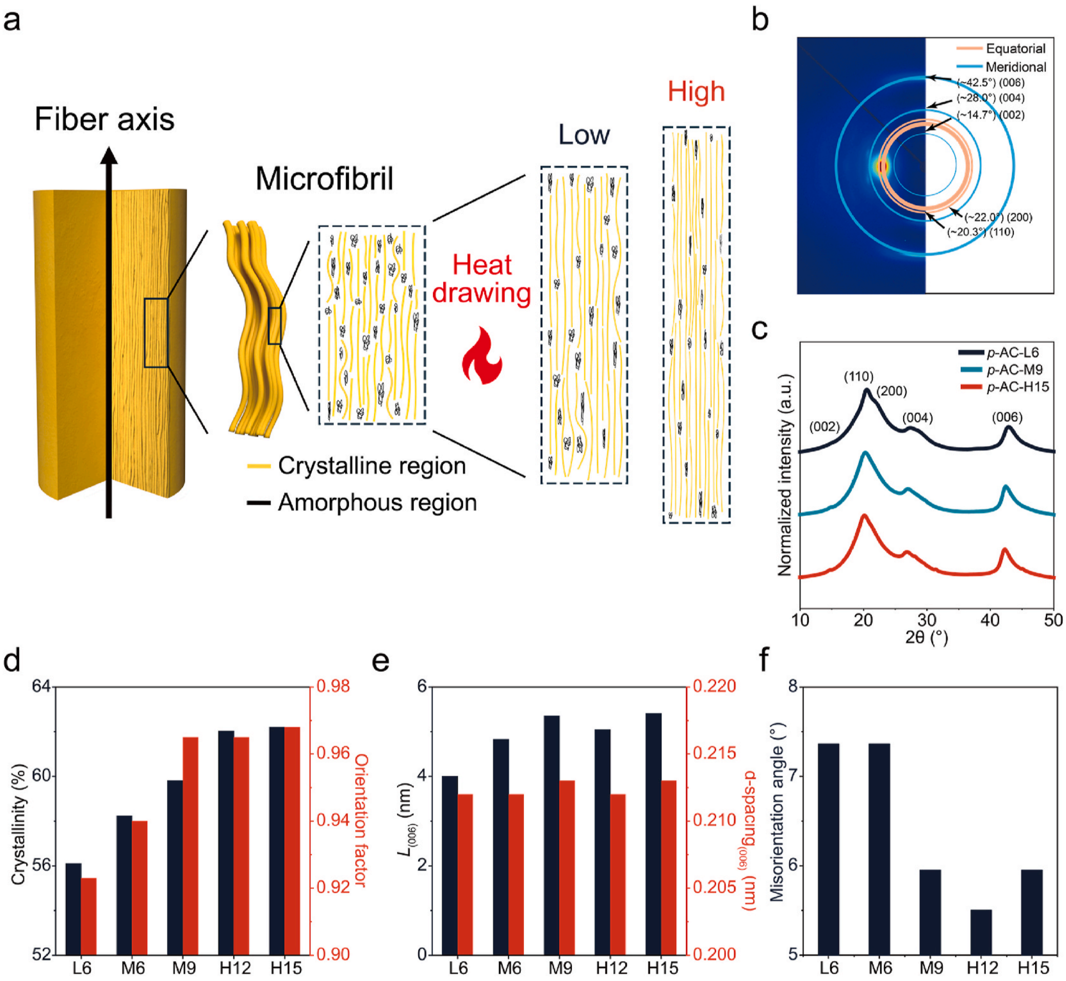

Fig. 4. Microstructure analysis of *p*-AC fibers. (a) Schematic explanation of crystalline structure of the *p*-AC, (b) representative 2D WAXD patterns of *p*-AC-L6, and (c) 1D WAXD profiles for the *p*-AC fibers. (d) Crystallinity and orientation factor of the *p*-AC fibers, (e) crystal size and d-spacing of (006) plane, and (f) misorientation angle of fibril structures from SAXS analysis.

microstructural factors observed in *p*-AC-L6 fibers confirmed that the poor morphological uniformity of the fibers was associated with reduced the microstructural perfection. At an identical TDR of 6, meanwhile, the *p*-AC-M6 fiber exhibited greater crystallinity and orientation factor than *p*-AC-L6, suggesting that the homogeneity of the spinning solution is another significant determinant of the microstructural evolution.

To investigate detailed changes in the crystalline structure, the crystal size and d-spacing of the (006) plane ($L_{(006)}$ and d-spacing$_{(006)}$) were examined, revealing sharp and intense peaks that became pronounced with increasing draw ratio. The (006) plane was selected for analysis because the diffraction peaks near 2θ ~ 20.3° showed no significant differences between *p*-AC-M9 and *p*-AC-H15, making the (006) near 2θ ~ 42.5° peak ideal for observing distinct structural differences. As the draw ratio increased, enhanced stretching along the fiber axis led to an increase in the $L_{(006)}$ value from 4.00 to 5.41 nm, consistent with the trends in crystallinity and the orientation factor (Fig. 4(e)). Interestingly, the d-spacing$_{(006)}$ was barely influenced by the draw ratio. This is because the d-spacing is determined by the intrinsic chemical structure of repeating units of the polymer and the fixed geometry of the crystal lattice, which is unaffected by the draw ratio [39]. Similar to the WAXD data, SAXS data showed that the misorientation angle of fibril structures reduced from 7.36 % (*p*-AC-L6) to 5.95 % (*p*-AC-H15), confirming that the increased crystallinity and orientation of crystal structures are extended to the enhanced alignment of microfibrils in the fibers (Fig. 4(f)–S4, S5, and Table 1).

3.5. Mechanical performance of p-AC fibers

Fig. 5 and Table 2 present the tensile properties of *p*-AC fibers in relation to their microstructural characteristics. The stress–strain curves indicate that the mechanical properties of *p*-AC fibers improved in the order of *p*-AC-L, *p*-AC-M, and *p*-AC-H fibers, which corresponds to the

Table 1
Structural properties of *p*-AC fibers analyzed by WAXD and SAXS.

Sample	Crystallinity (%)	Orientation factor	Misorientation angle (°)	$L_{(006)}$ (nm)	d-spacing$_{(006)}$ (nm)
p-AC-L6	56.1	0.923	7.36	4.00	0.212
p-AC-M6	58.2	0.940	7.36	4.83	0.212
p-AC-M9	59.8	0.965	5.95	5.35	0.213
p-AC-H12	62.0	0.965	5.50	5.04	0.212
p-AC-H15	62.2	0.968	5.95	5.41	0.213

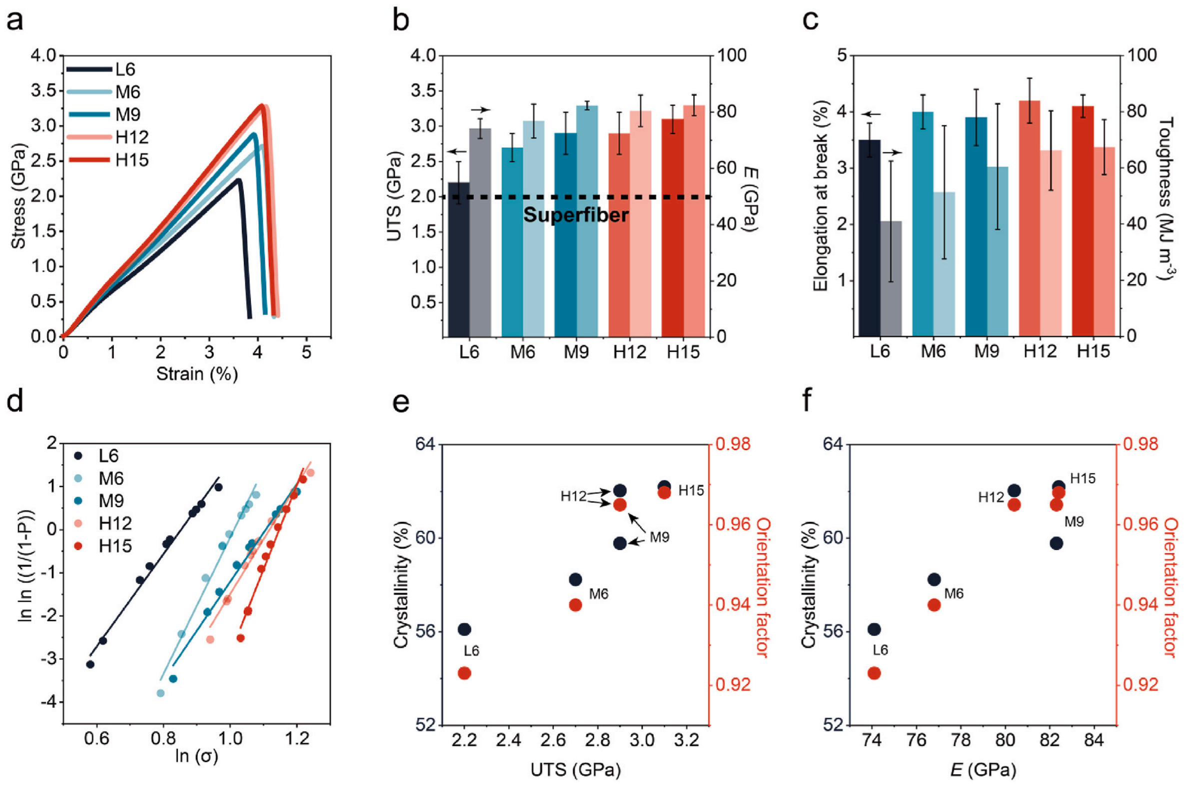

Fig. 5. Tensile properties of *p*-AC fibers. (a) Stress–strain curves of the *p*-AC fibers, (b) and (c) tensile properties. (d) Weibull plots of the *p*-AC fibers, (e) and (f) structural properties and tensile properties.

Table 2
Tensile properties of *p*-AC fibers.

Sample	Elongation (%)	Tensile strength (GPa)	Tensile modulus (GPa)	Toughness (MJ/m3)	Weibull modulus
p-AC-L6	3.5 ± 0.3	2.2 ± 0.3	74.1 ± 3.5	41.0	10.7
p-AC-M6	4.0 ± 0.3	2.7 ± 0.2	76.8 ± 6.0	51.3	15.8
p-AC-M9	3.9 ± 0.5	2.9 ± 0.3	82.3 ± 1.5	60.5	11.4
p-AC-H12	4.2 ± 0.4	2.9 ± 0.3	80.4 ± 5.6	66.2	12.7
p-AC-H15	4.1 ± 0.2	3.1 ± 0.2	82.4 ± 3.7	67.4	19.7

trend of spinning solution homogeneity (Fig. 5(a)). While the TDR is a significant factor in determining the final fiber properties, the degree of fiber drawing is fundamentally influenced by both the fiber morphology and solution homogeneity, as discussed earlier. Tensile modulus (*E*), ultimate tensile strength (UTS), elongation at break (ε_b), and toughness (*U*) were compared for the three *p*-AC fibers (Fig. 5(b) and (c)). Considering the property criteria of superfibers, defined as having *E* and UTS values of at least 50.0 and 2.0 GPa, respectively, all *p*-AC-L, *p*-AC-M, and *p*-AC-H fibers surpass these thresholds and can be classified as superfibers [40]. Notably, the *p*-AC-H15 fibers exhibited an *E* and UTS of 82.4 and 3.1 GPa, surpassing the criteria by 64.8 % and 55.0 %, respectively. Moreover, in terms of ε_b and *U* (Fig. 5(c)), the *p*-AC-H fibers exhibited the highest values among the fibers, with the *p*-AC-H15 fibers achieving ε_b of 4.1 % and *U* of 67.4 MJ m^{-3}. Typically, polymeric materials, including fibers, exhibited a trade-off between stiffness (i.e., *E*) and stretchability (i.e., ε_b) [41]. In contrast to the theoretical trade-off, interestingly, *p*-AC-H12 and -H15 fibers outperformed the *p*-AC-L6 fibers in both mechanical aspects (Fig. 5(b) and (c)). In particular, the *p*-AC-H15 fibers demonstrated a *U* value of 67.4 MJ m^{-3}, which was nearly 1.5 times higher than that of the *p*-AC-L6 fibers (41.0 MJ m^{-3}). These results confirm that enhancing the structural uniformity by optimizing the spinning solution properties is one of the most effective strategies for maximizing the overall performance of superfibers.

The Weibull modulus was derived from the distribution of defects in the fibers, which influenced the tensile strength (Fig. 5(d)) [42,43]. A significant increase in the Weibull modulus from 10.7 (*p*-AC-L6 fibers) to 19.7 (*p*-AC-H15 fibers) was in line with the reduction in structural defects. In particular, while the Weibull modulus of commercial superfibers such as Kevlar® and Technora® range from 10.0 to 13.2, the *p*-AC-H15 fibers considerably surpass this modulus by 6.5, demonstrating superior structural homogeneity [43]. In this regard, improving the solution quality can enhance not only the tensile properties but also the reliability of the fracture behavior. The effects of the morphological structures on fiber properties, as well as a correlation between the microstructural factors and mechanical performances are depicted in Fig. 5(e) and (f). Both microstructural parameters, crystallinity and orientation factor, exhibited a substantial proportion with *E* and UTS in the case of *p*-AC-L and *p*-AC-M fiber groups; however their influence diminished in the *p*-AC-H fibers. This suggests that microstructural evolution reaches saturation at a TDR of 12 for *p*-AC-H fibers and that further improvements in mechanical properties are primarily attributed to reduced structural defects through additional drawing, as supported by the increased Weibull modulus.

In addition to mechanical performance, the *p*-AC fibers also demonstrated superior thermal stability and durability, confirming the classification as superfibers. Regardless of the solution homogeneity, all three types of fibers showed excellent heat resistance, with no significant degradation observed at temperatures above 400 °C in air (Fig. S6). The durability of the *p*-AC fibers was evaluated from the perspectives of their creep and fatigue behaviors (Fig. 6(a)). The dimensional stability of the fiber was measured at a constant stress in the creep test, while it was recorded during cyclic stress loading and unloading in the fatigue test.

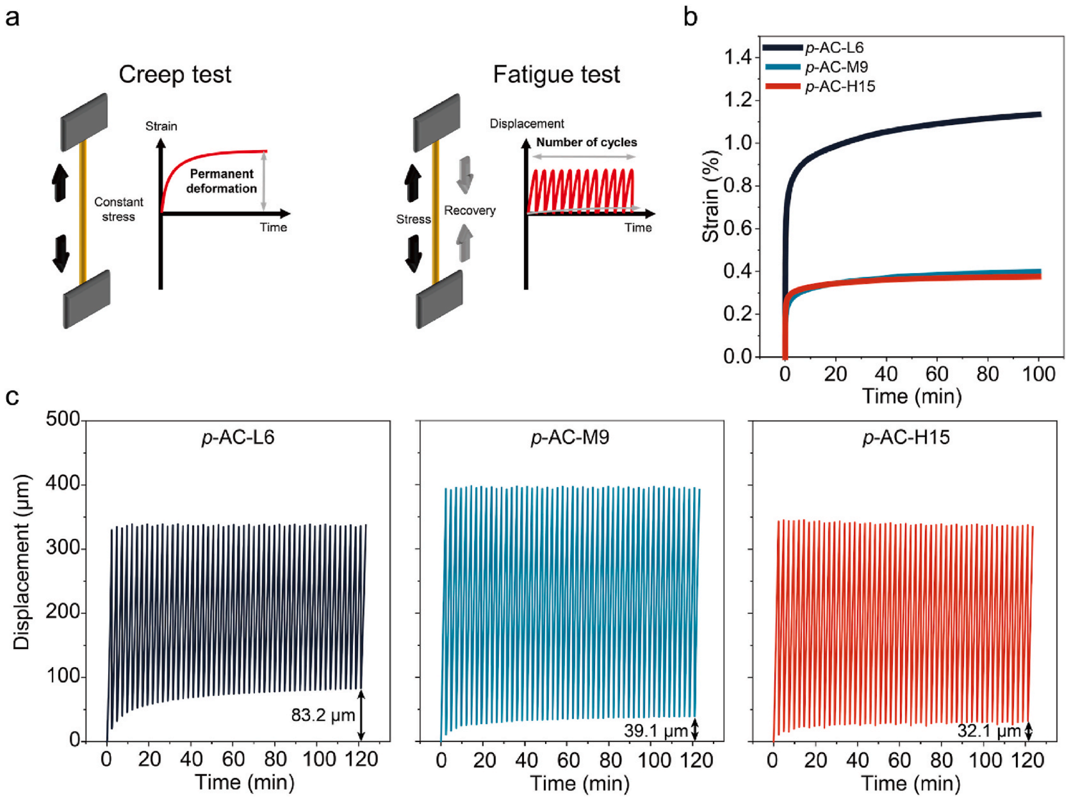

Fig. 6. Durability tests of *p*-AC fibers. (a) Schematic representation of creep and fatigue tests. (b) Creep test at 40 % tensile strength, and (c) cycle test with 50 cycles at 50 % tensile strength.

Lower strain under constant stress reflected the dimensional stability of fibers; however, *p*-AC-L6 exhibited a strain of 1.13 %, which was higher than that of *p*-AC-M9 (0.40 %) and *p*-AC-H15 (0.38 %) (Fig. 6(b)). The higher the grade, the smaller the displacement was measured. In the cyclic tests, the displacements were compared after 50 tensile tests were completed. The displacement of *p*-AC-L6 was 83.2 μm, about 2.5 times larger than that of *p*-AC-H15 (32.1 μm), while *p*-AC-M9 exhibited a displacement of 39.1 μm, slightly larger than *p*-AC-H15 (Fig. 6(c)). The internal structure of the fibers was affected by structural changes not only in the one-time tensile test, but also under repeated or constant external force conditions. These two tests suggest that permanent deformation is larger in fibers with lower crystallinity, indicating that the amorphous regions in the fiber are affected by repeated or constant stress.

4. Conclusions

In this study, the mechanical performance of p-AC fibers, regarded as superfibers, was optimized by elucidating the correlations among solution properties, fiber structure, and final fiber properties. In particular, higher molecular weight combined with improved solution homogeneity synergistically enhanced structural uniformity, resulting in superior mechanical properties of *p*-AC fibers. Throughout the manufacturing process, the processing and structural parameters of the *p*-AC fibers were found to be strongly interconnected in the following sequence: 1) neutralization time of the polymerization stage → 2) spinning solution homogeneity → 3) uniformity of the as-spun fibers and the extent of drawing → 4) final fiber properties. The *p*-AC fibers prepared from more homogeneous spinning solutions exhibited higher draw ratios, improved crystallinity, and greater molecular orientation. As a result, the *p*-AC-H15 fibers (E and UTS of 82.4 and 3.1 GPa, respectively) achieved up to 41.0 % higher tensile strength and 11.2 % higher modulus compared to *p*-AC-L6 fibers. Moreover, they outperformed the criteria of superfibers (E and UTS of 50.0 and 2.0 GPa, respectively) by 64.8 % and 55.0 %, respectively. These results confirm that controlling the solution homogeneity and molecular weight is key to enhancing fiber performance. This approach provides a practical and scalable pathway for producing next-generation *p*-AC superfibers with superior mechanical properties and offer an effective alternative to conventional *p*-aramid processing.

CRediT authorship contribution statement

Jaegeun Lyu: Writing – review & editing, Writing – original draft, Visualization, Formal analysis, Data curation. **Hyeonjeong Kim:** Writing – original draft, Visualization, Data curation. **Min Woo Kim:** Formal analysis. **Juyoung Kim:** Formal analysis. **Howon Choi:** Formal analysis. **Donghoon Lee:** Formal analysis. **Daeyoung Lim:** Formal analysis. **Ji Ho Youk:** Writing – review & editing, Supervision, Conceptualization. **Youngho Eom:** Writing – review & editing, Writing – original draft, Supervision, Funding acquisition, Data curation, Conceptualization. **Han Gi Chae:** Writing – review & editing, Writing – original draft, Supervision, Project administration, Funding acquisition, Conceptualization.

Declaration of competing interest

The authors declare that they have no known competing financial interests or personal relationships that could have appeared to influence the work reported in this paper.

Acknowledgements

This work was supported by the National Research Foundation of Korea (2021M3H4A3A01043764) and the Nano & Material Technology Development Program through the National Research Foundation of Korea (NRF) funded by Ministry of Science and ICT (RS-2025-

25442298).

Appendix A. Supplementary data

Supplementary data to this article can be found online at https://doi.org/10.1016/j.polymertesting.2025.108987.

Data availability

Data will be made available on request.

References

[1] K. Friedrich, A.A. Almajid, Manufacturing aspects of advanced polymer composites for automotive applications, Appl. Compos. Mater. 20 (2013) 107–128.

[2] D. Shelly, S.-Y. Lee, S.-J. Park, Compatibilization of ultra-high molecular weight polyethylene (UHMWPE) fibers and their composites for superior mechanical performance: a concise review, Compos. B Eng. 275 (2024) 111294.

[3] J.H. Park, G.C. Rutledge, 50th anniversary perspective: advanced polymer fibers: high performance and ultrafine, Macromolecules 50 (2017) 5627–5642.

[4] H.G. Chae, S. Kumar, Making strong fibers, Science 319 (2008) 908–909.

[5] J.M. García, F.C. García, F. Serna, J.L. de la Peña, High-performance aromatic polyamides, Prog. Polym. Sci. 35 (2010) 623–686.

[6] A. He, T. Xing, Z. Liang, Y. Luo, Y. Zhang, M. Wang, Z. Huang, J. Bai, L. Wu, Z. Shi, Advanced aramid fibrous materials: fundamentals, advances, and beyond, Adv. Fiber Mater. 6 (2024) 3–35.

[7] S. Zhou, X. Wang, W. Zhang, M. Zhang, X. Zhang, N. Zhao, R. Liu, J. Xu, Z. Shen, X. Fan, Facile preparation and characterization of soluble aramid, J. Appl. Polym. Sci. 135 (2018) 4634159.

[8] Y. Liu, S. Zhou, N. Zhao, J. Xu, Z. Shen, X.-H. Fan, Q.-F. Zhou, Facile synthesis and characterization of soluble aramid containing polar hydroxyl side group, Polymer 238 (2022) 124411.

[9] H. Jeong, J. Lyu, H. Choi, M.W. Kim, J. Kim, H. Yoo, Y. Lee, J.H. Youk, H.G. Chae, Enhanced thermal conductivity and mechanical property via improvement of hydrogen bonding between hexagonal boron nitride and aramid copolymer, Compos. Sci. Technol. 253 (2024) 110652.

[10] Z. Zhang, P. Liu, Z. Li, Y. Li, X. Deng, H. Zhu, X. Liu, Q. Huang, L. Luo, Regulating polymer-solvent interactions to tune rheological behavior and enhance the spinnability of heterocyclic aromatic polyamide solutions, Polymer 324 (2025) 128229.

[11] F. Sloan, Liquid crystal aromatic polyester-arylate (LCP) fibers: structure, properties, and applications, in: Structure and Properties of high-performance Fibers, Elsevier, 2017, pp. 113–140.

[12] Y. Eom, D.E. Jung, S.S. Hwang, B.C. Kim, Characteristic dynamic rheological responses of nematic poly (p-phenylene terephthalamide) and cholesteric hydroxypropyl cellulose phases, Polym. J. 48 (2016) 869–874.

[13] R. Xu, Y. Qiu, S. Tang, C. Yang, Y. Dai, D. Zhang, Y. Gao, K. Gao, L. Luo, X. Liu, Preparation of high strength and toughness aramid fiber by introducing flexible asymmetric monomer to construct misplaced-nunchaku structure, Macromol. Mater. Eng. 306 (2021) 2000814.

[14] L. Luo, Y. Yuan, Y. Dai, Z. Cheng, X. Wang, X. Liu, The novel high performance aramid fibers containing benzimidazole moieties and chloride substitutions, Mater. Des. 158 (2018) 127–135.

[15] D.E. Jung, H.J. Kim, D.W. Chae, B.C. Kim, Y. Eom, Rheological and morphological evidence of binary liquid crystalline phases in solutions of an organo-soluble cyano-substituted p-aramid, Polymer 260 (2022) 125357.

[16] C. Yang, H. Wu, Y. Dai, D. Zhang, R. Xu, L. Luo, X. Liu, Constructing mainstay-body structure in heterocyclic aramid fiber to simultaneously improve tensile strength and toughness, Compos. B Eng. 202 (2020) 108411.

[17] K. Akato, G. Bhat, High performance fibers from aramid polymers, in: Structure and Properties of high-performance Fibers, Elsevier, 2017, pp. 245–266.

[18] A. Dodero, S. Vicini, M. Alloisio, M. Castellano, Sodium alginate solutions: correlation between rheological properties and spinnability, J. Mater. Sci. 54 (2019) 8034–8046.

[19] B.A. Newcomb, P.V. Gulgunje, Y. Liu, K. Gupta, M.G. Kamath, C. Pramanik, S. Ghoshal, H.G. Chae, S. Kumar, Polyacrylonitrile solution homogeneity study by dynamic shear rheology and the effect on the carbon fiber tensile strength, Polym. Eng. Sci. 56 (2016) 361–370.

[20] N. Komiya, Method for Producing copolyparaphenylene-3,4'-oxydiphenylene Terephthalamide Fiber, Japan, 2015.

[21] S. Hayashida, Technora® fiber: super fiber from the isotropic solution of rigid-rod polymer, in: High-Performance and Specialty Fibers: Concepts, Technology and Modern Applications of Man-Made Fibers for the Future, 2016, pp. 149–169.

[22] S. Krimm, A.V. Tobolsky, Quantitative x-ray studies of order in amorphous and crystalline polymers. Quantitative x-ray determination of crystallinity in polyethylene, J. Polym. Sci. 7 (1951) 57–76.

[23] Z.W. Wilchinsky, Recent developments in the measurement of orientation in polymers by X-ray diffraction, Adv. X Ray Anal. 6 (1962) 231–241.

[24] J.L. White, J.E. Spruiell, The specification of orientation and its development in polymer processing, Polym. Eng. Sci. 23 (1983) 247–256.

[25] R. Perret, W. Ruland, The microstructure of PAN-base carbon fibres, J. Appl. Crystallogr. 3 (1970) 525–532.

[26] K. Şahin, J. Clawson, J. Singletary, I. Chasiotis, Shear strength of homopolymer and copolymer aramid fibers, Polymer 186 (2020) 122034.

[27] Y. Dai, Z. Cheng, C. Meng, Y. Yuan, L. Luo, X. Liu, Dissolution of aramid by ionization of byproduct HCl promoted by acetate, ChemistrySelect 4 (2019) 123–129.

[28] Y. Dai, Z. Cheng, Y. Yuan, C. Meng, J. Qin, X. Liu, In situ complex with by-product HCl and release chloride ions to dissolve aramid, ChemPhysChem 19 (2018) 2468–2471.

[29] L. Yao, C. Lee, J. Kim, Fabrication of electrospun meta-aramid nanofibers in different solvent systems, Fibers Polym. 11 (2010) 1032–1040.

[30] H. Kim, H.J. Kim, Y. Lee, J.K. Kim, Y. Eom, Rheological characterization of cellulose nanocrystal-laden self-healable polyvinyl alcohol hydrogels, Korea Aust. Rheol. J. 35 (2023) 31–38.

[31] M. Shin, S.-H. Shin, M. Lee, H.J. Kim, J.H. Jeong, Y.H. Choi, D.X. Oh, J. Park, H. Jeon, Y. Eom, Rheological criteria for distinguishing self-healing and non-self-healing hydrogels, Polymer 229 (2021) 123969.

[32] J. Stetefeld, S.A. McKenna, T.R. Patel, Dynamic light scattering: a practical guide and applications in biomedical sciences, Biophysical Rev. 8 (2016) 409–427.

[33] N. Farkas, J.A. Kramar, Dynamic light scattering distributions by any means, J. Nanoparticle Res. 23 (2021) 120.

[34] A. Ziabicki, R. Takserman-Krozer, Effect of rheological factors on the length of liquid threads, Colloid Polym. Sci. 199 (1964) 9–13.

[35] L. Tan, H. Chen, D. Pan, N. Pan, Investigating the spinnability in the dry-jet wet spinning of PAN precursor fiber, J. Appl. Polym. Sci. 110 (2008) 1997–2000.

[36] R. Tomisawa, T. Ikaga, K. Kim, Y. Ohkoshi, K. Okada, H. Masunaga, T. Kanaya, M. Masuda, Y. Maeda, Effect of draw ratio on fiber structure development of polyethylene terephthalate, Polymer 116 (2017) 357–366.

[37] A. Hindeleh, S.M. Abdo, Effects of annealing on the crystallinity and microparacrystallite size of Kevlar 49 fibres, Polymer 30 (1989) 218–224.

[38] K.G. Lee, R. Barton Jr., J. Schultz, Structure and property development in poly (p-phenylene terephthalamide) during heat treatment under tension, J. Polym. Sci., Part B: Polym. Phys. 33 (1995) 1–14.

[39] S. Ran, D. Fang, X. Zong, B. Hsiao, B. Chu, P.M. Cunniff, Structural changes during deformation of Kevlar fibers via on-line synchrotron SAXS/WAXD techniques, Polymer 42 (2001) 1601–1612.

[40] Y. Hua, Y.-C. Yang, A. Yamanaka, Q.-Q. Ni, Low friction coefficient property of super fiber-reinforced composites, Adv. Compos. Mater. 20 (2011) 133–147.

[41] D. Johnson, Structure-property relationships in carbon fibres, J. Phys. D Appl. Phys. 20 (1987) 286.

[42] K. Naito, J.-M. Yang, Y. Tanaka, Y. Kagawa, The effect of gauge length on tensile strength and Weibull modulus of polyacrylonitrile (PAN)-and pitch-based carbon fibers, J. Mater. Sci. 47 (2012) 632–642.

[43] K. Naito, Tensile properties and weibull modulus of some high-performance polymeric fibers, J. Appl. Polym. Sci. 128 (2013) 1185–1192.